The ^{13}C Solid DNP Mechanisms with Perchlorotriphenylmethyl Radicals – the Role of ^{35,37}Cl

F. Mentink Vigier[a], D. Shimon[a], V. Mugnaini[b,c], J. Veciana[b,c] A. Feintuch[a], M. Pons[d], S. Vega[a], D. Goldfarb[a].

[a]Chemical Physics Department Weizmann Institute of Science 76100 Rehovot, Israel, [b]Institut de Ciencia de Materials de Barcelona (ICMAB-CSIC), Bellaterra, Spain, [c]Networking Research Center on Bioengineering, Biomaterials, and NanoMedicine (CIBER-BBN), Bellaterra, Spain, [d]Biomolecular NMR laboratory, Department of Organic Chemistry, University of Barcelona, Baldiri Reixac, 10-12 08028 Barcelona, Spain.

*corresponding author: daniella.goldfarb@weizmann.ac.il

Abstract

The microwave frequency swept DNP enhancement, referred to as the DNP spectrum, is strongly dependent on the EPR spectrum of the polarizing radical and it reveals the underlying DNP mechanisms. Here we focus on two chlorinated trityl radicals that feature axially symmetric powder patterns at 95 GHz, the width of which are narrower than those of TEMPOL or TOTAPOL but broader than that of the Trityl derivative OX63. The static DNP lineshapes of these commonly used radicals in DNP, have been recently analyzed in terms of a superposition of basic Solid Effect (SE) and Cross Effect (CE) - DNP lineshapes, with their relative contributions as a fit parameter. To substantiate the generality of this approach and further investigate an earlier suggestion that a ^{35,37}Cl - ^{13}C polarization transfer pathway, termed "hetero-nuclear assisted DNP", may be in effect in the chlorinated radicals (C. Gabellieri et al, *Angew. Chem. Int.,*49, 3360–2, 2010), we measured the static ^{13}C-glycerol DNP spectra of solutions of ca. ~ 10 mM of the two chlorinated Trityl radicals as a function of temperature (10 - 50 K) and microwave power. Analysis of the DNP lineshapes was first done in terms of the SE/CE superposition model calculated assuming a direct e - ^{13}C polarization transfer. The CE was found to prevail at the high temperature range (40 - 50 K), whereas at the low temperature end (10 - 20 K) the SE dominates, as it was observed earlier for ^{13}C DNP with OX63 and ^{1}H DNP with TEMPOL and TOTAPOL, thus indicating that this is rather general behavior. Furthermore, it was found that at low temperatures it is possible to suppress the SE, and increase the CE by merely lowering the microwave power. While this analysis gave a good agreement between experimental and calculated lineshapes when the CE dominates, some significant discrepancies were observed at low temperatures, where the SE dominates. We show that by explicitly taking into account the presence of $^{35/37}$Cl nuclei through a e - ^{35,37}Cl - ^{13}C polarization pathway in the SE-DNP lineshape calculations, as proposed earlier, we can

improve the fit significantly, thus supporting the existence of the "hetero-nuclear assisted DNP" pathway.

Introduction

DNP (dynamic nuclear polarization) is a process by which NMR signals are enhanced by transfer of polarization from electron spins to nuclear spins, achieved *via* the microwave (MW) irradiation of the electron spins. Several polarization transfer mechanisms can lead to DNP in the solid state: the Overhauser Effect[1,2], the Solid Effect (SE)[3–6], the Cross Effect (CE) [7–10] and Thermal Mixing (TM) [11–13]. In general, at very low temperatures, the last three mechanisms are the most commonly observed. They can be distinguished by the number of electron spins involved in the process and they can be identified by the characteristics of the DNP spectra, i.e. the enhancement of the NMR signal as a function of the MW irradiation frequency. The SE mechanism takes place when single electrons polarize their neighboring nuclei [3] and it is characterized by a frequency swept DNP spectrum that is broader than the EPR spectrum of the polarizing radicals by about twice the nuclear Larmor frequency. The CE mechanism occurs when pairs of coupled electrons polarize the nuclei [7,8] and the DNP spectral width is the same as that of the EPR spectrum. Finally, the nuclear polarization enhancement during TM takes place when spin thermodynamics accounts for the polarization transfer between multi-electron spin coupled systems and the nuclei [11,12]. It manifests itself by the observation that the DNP spectra are independent on the type of the nuclei observed. Which mechanism prevails under which conditions is still not a fully understood issue. This seems to depend on the nature of the radical used, its concentration, the temperature, the EPR spectrum's characteristics, the electron and nuclear spins Larmor frequencies and associated relaxation times.

In a series of recent works, carried out on a home built 95 GHz spectrometer that focused on the lineshape analysis of the DNP spectra, it has been shown that under static conditions and in the temperature range of 6 - 60 K, for radical concentrations of 5 - 40 mM the CE and SE are the underlying mechanisms. Moreover, the CE mechanism dominates at the high temperature (30 - 60K) whereas the SE takes charge at the low temperature range (6 - 10K) [14] [15]. This behavior was observed for ^{13}C enhancement using OX63 (Trityl) radical [14] and for ^{1}H enhancement with the nitroxide based radicals, TEMPOL, which is a mono-radical[15], and TOTAPOL, which is a bi-radical derivative[16]. Although the reason for the prevalence of the

2

SE at low temperature under sufficiently high power conditions is not fully understood, it was suggested that it is a consequence of the long nuclear relaxation time. 95 GHz DNP measurements are relevant as this is the frequency at which most of the low temperature dissolution DNP experiments are performed[17–19]. Recently home built spectrometers have been developed in order to characterize the DNP process at MW frequencies of 140 GHz and 200 GHz at field strengths of 5 T[20] and 7 T[21], respectively. Interestingly, at 200 GHz, in the temperature range of 3.7 K to 35 K and with rather low power, the CE was found to be the dominating mechanism for static ^{13}C-DNP with OX63 [21].

In this article we focus on the static ^{13}C-DNP mechanism of two carbon centered perchloro-triphenylmethyl radicals (1 and 2 in Figure 1), the structures of which are similar to that of the commercially available OX63, and introduced as DNP polarizers for dissolution DNP [22]. Our goal is further understanding the generality of the coexistence of the SE and CE and of the factors that determine their interplay. The reason for choosing these radicals is twofold. First, they exhibit EPR lineshapes that differ from earlier studied radicals. These lineshapes are rather simple axially symmetric powder patterns, and are broader than the nearly isotropic lineshape of OX63. In addition, they lack the complications in the lineshapes of nitroxides, which feature both resolved ^{14}N hyperfine and g-anisotropies. Second, and more importantly, these radicals contain chlorine atoms that can have an influence on the ^{13}C-DNP mechanisms. In an earlier work it was suggested that at very low temperatures (~ 1.5 K) the DNP mechanism is the SE mechanism, reinforced by {^{35,37}Cl → ^{13}C} polarization transfer referred to as "heteronuclear assisted DNP" [22–24]. It was further shown that there is a significant overlap between the ^{35,37}Cl and ^{13}C nuclear resonances that could facilitate the polarization transfer between the ^{35,37}Cl core nuclei and the bulk ^{13}C nuclei[24].

In the earlier study of the chlorinated radicals DNP lineshapes were recorded at only one temperature [24]. Here we follow the approach described above and focus on the variation of the DNP lineshapes with temperature and MW power and analyze them in terms of a superposition of characteristic SE- and CE-DNP lineshapes. The two shapes are derived from a theoretical approach based on simple small spin system calculations while taking relaxation and the EPR lineshape into account and ignoring electron-spin spectral diffusion effects. We found that again, as in the case of OX63, TEMPOL and TOTAPOL, in the range of 10-40 K both the SE and CE are effective: SE prevails at the low end and CE at the high end. In addition, reduction of the MW power abolished the SE, but not the CE. However, as already reported earlier, at the low temperature end DNP lineshapes could not be described

satisfactorily by the SE-DNP lineshape based on direct polarization transfer from an electron to the ^{13}C nuclei [24]. To improve the agreement with the experimental results we extend our simple two spin model and introduce the "heteronuclear assisted DNP" pathway {electron→^{35,37}Cl→^{13}C} into our calculations.
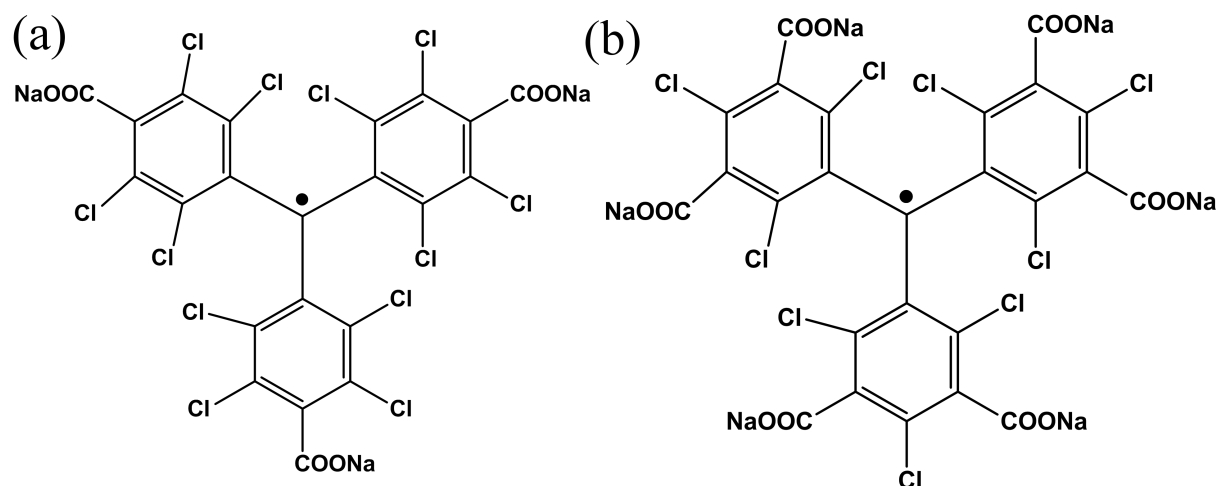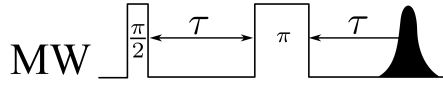
Experimental

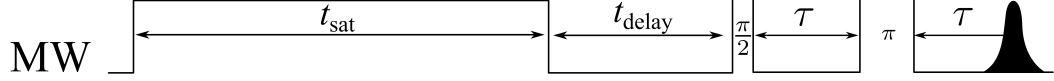**Fig. 1:** Structure of Radical 1 (a) and Radical 2 (b).

Sample preparation

Solutions of 11 ± 1 mM Radical 1 and 10 ± 1 mM Radical 2 (see Fig. 1) in doubly ^{13}C labeled glycerol (glycerol-1,3-^{13}C, 99 %, Cambridge Isotope Laboratories) and doubly distilled water (50/50 % in volume) were used for the DNP measurements. The radicals were synthesized as described previously [25,26]. The radical concentration was determined by spin counting experiments. Continuous wave EPR spectra were recorded at room temperature using a dual cavity and a Varian E-12 X-band upgraded spectrometer with a 1 mM OX63 solution as a reference. The EPR spectra of Radical 1 or Radical 2 were recorded simultaneously with the reference.

4

(a) EDEPR and Echo decay

MW pulse sequence: $\frac{\pi}{2}$ — τ — π — τ — echo

(b) Saturation recovery

MW pulse sequence: t_{sat} — t_{delay} — $\frac{\pi}{2}$ — τ — π — τ — echo

(c) DNP Sweep

MW: T_{DNP}

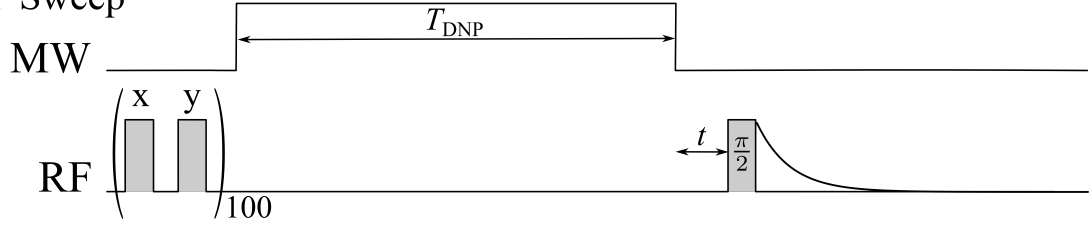RF: $\begin{pmatrix} x & y \end{pmatrix}_{100}$ ... t — $\frac{\pi}{2}$ — FID

Fig. 2: The pulse sequences used to characterize the samples. (a) Echo detection EPR (EDEPR): τ is kept constant and the magnetic field is swept. For phase memory time measurements, the echo decay is measured as a function of τ, while the magnetic field is fixed. (b) Saturation recovery experiment: t_{delay} is incremented. (c) DNP sequence: the microwave frequency is varied for each experimental point while monitoring the ^{1}H FID. For buildup measurements, T_{DNP} is increased while t and the microwave frequency are fixed. For a builddown measurement t is increased while T_{DNP} and the microwave frequency are fixed.

Spectroscopic measurements

EPR measurements were performed on a 94.9 GHz home built spectrometer [27] and the DNP measurements were carried out on a home built hybrid EPR – NMR spectrometer [27] at the same field. The echo detected EPR (EDEPR) spectra were recorded at 10 K using a $\pi/2 - 550$ ns $- \pi - 550$ ns – echo sequence (Fig. 2a) with pulse lengths of 100 ns and 200 ns respectively. The phase memory times, T_M, were measured by echo decay ($t_{\pi/2} = 30$ ns and $t_\pi = 60$ ns). The electron spin lattice relaxation, T_{1e}, was measured at 10 K by saturation recovery (Fig. 2b, $t_{sat} = 10$ ms, $t_{delay} = 10$ μs, $t_{\pi/2} = 30$ ns and a $t_\pi = 60$ ns, $\tau = 550$ ns). The T_{1e} and T_M measurements were carried out on the same solutions but on a home built pulse EPR spectrometer[28]

The DNP pulse sequence is described in Fig. 2c. The first part consists of a ^{13}C saturation pulse train (two radio – frequency (RF) pulses of 12 μs, one along x and the other along y, repeated 100 times) applied to eliminate the thermal nuclear polarization and to always start from the same initial condition. Then MW irradiation was applied, followed by a free induction decay (FID) detection after a $\pi/2$ RF pulse of 16 μs. The highest microwave power applied corresponds to $\omega_1/2\pi = 0.6$ MHz, as determined from electron spin nutation

measurements, and the lowest power applied was 0.06 MHz. Unless otherwise specified, the experiments were performed with the highest microwave power.

A DNP buildup experiment, where the NMR signal is measured as a function of the MW irradiation time, T_{DNP}, was carried out at 10 K. It showed that a steady state DNP signal is obtained in about 2000 s. DNP spectra were not measured at steady state but by setting T_{DNP} to a value that produced a good SNR in a reasonable amount of time. For Radical 1 T_{DNP} was set to 600 s in the range of 10 – 30 K, 800 s for 40 K and 1200 s for 50 K. For Radical 2 T_{DNP} was set to 800 s at 10 K, 600 s at 20 and 30 K, and 800 s at 40 and 50 K. The DNP lineshapes did not reveal a dependence on the irradiation time within the MW irradiation times used in this work. The irradiation times chosen were long enough to ensure sufficient SNR and that the DNP spectrum has reached its steady state lineshape.

A DNP decay experiment was also performed in order to obtain the nuclear spin lattice relaxation, T_{1n}. The sequence employed is very similar to that shown in Fig. 2c, setting the microwave frequency close to the maximum enhancement of the NMR signal. The sample was irradiated for 600 s and the NMR signal was then collected as a function of time after the end of the MW irradiation. The data were then fitted to a single exponential decaying function.

Eventually, the absolute enhancement value was measured at 20 K. The MW on - signal was recorded after irradiating for 2800 s (at steady state) with full microwave power ($\omega_1/2\pi \sim 0.6$ MHz). The off - signal was obtained with the same sequence but without MW irradiation. In order to achieve sufficient SNR, 58 scans were collected for the off - signal for both radicals. The FIDs were Fourier transformed and the integrals of the MW on- and off-signals were compared.

The DNP enhancement determined at 20 K was used to derive the enhancements at all other temperatures. This was done by estimating the intensity of the off-signals at these temperatures by scaling the off-signal at 20 K according to their relative Boltzmann factors and dividing the on-signals by these values.

Simulations

In order to interpret the frequency swept DNP data, we performed simulations of the nuclear polarization of small spin systems containing interacting electrons and nuclei. These simulations consist of computing the truncated spin Hamiltonian in the rotating frame of the

electron spin and diagonalizing it in order to introduce relaxation rates in the eigenbasis of these systems. The evolution of the spin system is then obtained by solving the Liouville Von Neuman equation in the presence of a MW field. In this work we used two different quantum mechanical models to account for the DNP spectra: (I) The first one was described previously[14–16] and relies on the computation of basic SE-DNP and CE-DNP spectra considering a direct polarization transfer from the electrons to a nucleus, in our case ^{13}C, using a three-spin model system {e⁻ – e⁻ – ^{13}C} along with a convolution with the experimental EPR spectrum of the radicals. (II) In the second model we compute SE-DNP spectra while taking the presence of $^{35,37}Cl$ into account by considering the polarization transfer in the three-spin system {e⁻ – $^{35(37)}Cl$ – ^{13}C}. This model is inspired from previous simulations [24] but it takes into account the presence of ^{13}C as well as the different relaxation processes. Moreover, a full powder averaging is performed taking the g-anisotropy parameters into account. Thus the EPR lineshape calculation was implicit in the simulation and no convolution with the experimental spectrum was used. Next we describe these two approaches in somewhat more details.

Model I:

The basic SE- and CE-DNP spectra were first simulated using the method presented by Shimon *et al.*[14–16]. In this method, both spectra are computed using a single $\{e_1^- - e_2^- - ^{13}C\}$ spin system placed in an external magnetic field with fixed electron-electron dipolar and electron-nuclear hyperfine interactions. This system has the following Hamiltonian in the MW rotating frame

$$\hat{H}_0^R = \sum_{i=1,2} \left(\Delta\omega_i S_{z,i} + A_{z,i}^C S_{z,i} I_z^C + A_{\pm,i}^C \left(S_{z,i} I_+^C + S_{z,i} I_-^C \right) \right) - g_n^C \beta_n^C B_0 I_z^C +$$

$$d_{1-2} \left(2 S_{z,1} S_{z,2} - S_{x,1} S_{x,2} - S_{y,1} S_{y,2} \right) + \omega_1 (S_{x,1} + S_{x,2}) \qquad (1)$$

where $\Delta\omega_i/2\pi$ are the off - resonance frequencies of electrons 1 and 2 and the operators representing the hyperfine and dipolar interaction are truncated such that they are secular with respect to the electron spin. In our calculations we have chosen $A_{z,i}^C/2\pi = 0$ MHz for simplicity and took for the pseudosecular coefficients $A_{\pm,2}^C/2\pi = 0$ MHz and $A_{\pm,1}^C/2\pi = 0.1$ MHz, corresponding to a core nucleus at a distance of 0.6 nm from an electron spin. In addition, a dipolar coefficient $d_{1-2}/2\pi = 0.4$ MHz, corresponding to a typical electron-electron distance of 5 nm in a sample with radical concentrations in the range ~ 10 - 15 mM, was chosen.

These simulations also take into account the electron and nuclear relaxation times, T_{1e}, T_{1n} and T_{2e} (approximated by T_m) and T_{2n}. The values used in the simulations were $T_{1e} = 50$ ms, $T_{2e} = 1$ μs, $T_{1n}(^{13}C) = 500$ s, $T_{2n}(^{13}C) = 1$ ms. The values of T_{1e} and T_m were measured for both radicals and were found to be somewhat different (see below). In the simulations we used an average value for both because in this range of values they do not influence the shape of the DNP profile. T_{1n} was also determined experimentally. As described in earlier publications[14], the DNP enhancement of the ^{13}C signal is calculated by solving the Liouville Von Neuman equation in the presence of MW irradiation for a variety of values of $\Delta\omega_1/2\pi$ and $\Delta\omega_2/2\pi$. This gives rise to a 2D profile of the enhancement as function of these two frequencies. This profile has clear regions where the SE and the CE are operative. The two areas of this 2D profile associated with the CE and the SE enhancements were then determined and each was convoluted with the EPR lineshape. This procedure resulted in two distinct DNP spectra: the basic normalized SE and the CE spectra. The area belonging to the CE was determined by choosing a frequency band with a width of 7 MHz around the positions of the CE conditions. The order of magnitude of the width is determined by the frequency spread of the CE conditions, influenced by the hyperfine and dipolar interactions in the sample, and off-resonance effects. Changing the width by a factor of 2 has a very small effect on the CE line shape. The 2D profile outside the CE area determined the SE enhancement[14]. To fit the experimental DNP spectra the basic CE and SE lineshapes are added with a different relative intensity as a fitting parameter.

This method has been successfully applied to the ^1H-DNP spectra of TEMPOL containing samples and the ^{13}C-DNP spectra of OX63 samples. It appeared to be a robust method for evaluating the relative contributions of the two DNP mechanisms as a function of temperature [14,15]. In the case of TOTAPOL a slight modification of the SE lineshape was necessary to obtain a good fit[16].

Model II:

Here the basic ^{13}C SE-DNP spectra were re-evaluated by considering a three spins system containing one electron coupled to a chlorine nucleus, which is coupled to a ^{13}C nucleus : {e⁻ − ^{35}Cl − ^{13}C} (the ^{13}C is not coupled to the electron spin directly). ^{35}Cl was chosen as an example representing both isotopes $^{35,37}Cl$. The laboratory frame Hamiltonian with the magnetic field in the z-direction is given by:

$$\hat{H}_0 = \beta_e \vec{B}_0 g S - g_n^C \beta_n^C B_0 I_z^C - g_n^{Cl} \beta_n^{Cl} B_0 I_z^{Cl} + S\, A_z^{Cl} I^{Cl} + I^{Cl} Q I^{Cl} + I^{Cl} d_{Cl-C} I^C \quad (2),$$

This Hamiltonian is then transformed into the rotating frame of the MW irradiation at frequency, ω_{mw}, where the diagonal electron Zeeman term is characterized by a $g(\Omega)$ value dependent on the g-tensor orientation (Ω). In this Hamiltonian the hyperfine term is truncated with respect to the electron Zeeman term and the ^{35}Cl-^{13}C dipolar term with respect to the nuclear Zeeman terms. After the addition of the MW irradiation this Hamiltonian gets the form

$$\hat{H}_0^R = (\beta_e B_0 g(\Omega) - \omega_{mw}) S_z - g_n^C \beta_n^C B_0 I_z^C - g_n^{Cl} \beta_n^{Cl} B_0 I_z^{Cl} + A_z^{Cl} S_z I_z^{Cl} +$$
$$(A_+^{Cl} I_+^{Cl} + A_-^{Cl} I_-^{Cl}) S_z + I^{Cl} Q I^{Cl} + 2 d_{Cl-C} I_z^{Cl} I_z^C + \omega_1 S_x \qquad (3)$$

The ^{13}C polarization enhancements are calculated as a function of the orientation of a three-spin system with well-defined g, $^{35/37}$Cl hyperfine- and quadrupolar tensor parameters. The g-tensor parameters were derived from the EPR spectra (g = [2.00338, 2.00074, 2.0002], for Radical 1), and the hyperfine and the quadrupolar interaction components and their fixed relative orientations with respect to the g-tensor were previously calculated by DFT [24]. A comparison of experimental ELDOR detected NMR spectra and simulated ENDOR spectra showed that these parameters reproduced rather well the Radical 1 and Radical 2 experimental data [24]. Powder averaging was carried out by adding the results of 1154 orientations (ZCW crystal orientation file [29–31]) of the g-tensor with respect to the external magnetic field. For simplicity the ^{35}Cl – ^{13}C dipolar coupling was fixed at 1 kHz, corresponding to a distance of 0.3 nm.

The relaxation parameters chosen for the simulations were the same as those used for the first simulation method with the addition of T_{1n} ($^{35/37}$Cl) = 4 s for both radicals and both Cl isotopes, ^{37}Cl (25%) and ^{35}Cl (75%). The microwave amplitude was set to $\omega_1/2\pi$ = 0.6 MHz, determined experimentally by electron spin nutation measurements. In general variations of the relaxation time values used hardly affected the shape of the simulated DNP spectra, except for T_{1n} (^{35,37}Cl), which causes a broadening of the spectra when chosen larger than 10 s.

Results

Temperature dependence of the DNP spectra

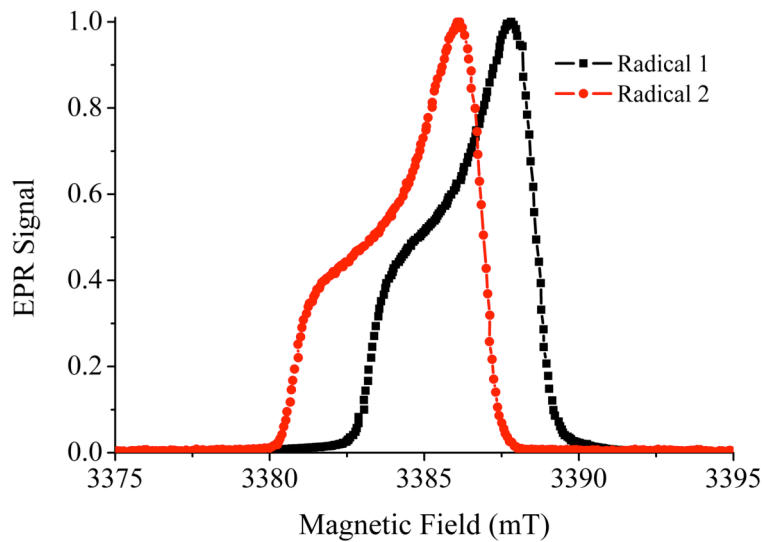Figure 3 presents the EDEPR spectra of Radicals 1 and 2, recorded at 10 K. As reported in

Fig. 3: W-band EDEPR spectrum of Radical 1 (black squares) and Radical 2 (red circles) recorded at 10 K

[22] for these two radicals, the EPR lineshapes are characteristic of axially symmetric g-tensors. The relaxation times, measured at 10 K and the $g_\perp$ position, were $T_M \sim 1$ µs and $T_{1e} = 30$ ms for Radical 1 and $T_M \sim 550$ ns and $T_{1e} = 80$ ms for the Radical 2. The bulk ^{13}C T_{1n} for Radical 1 and 2 was of the order of 500 ± 100 s.
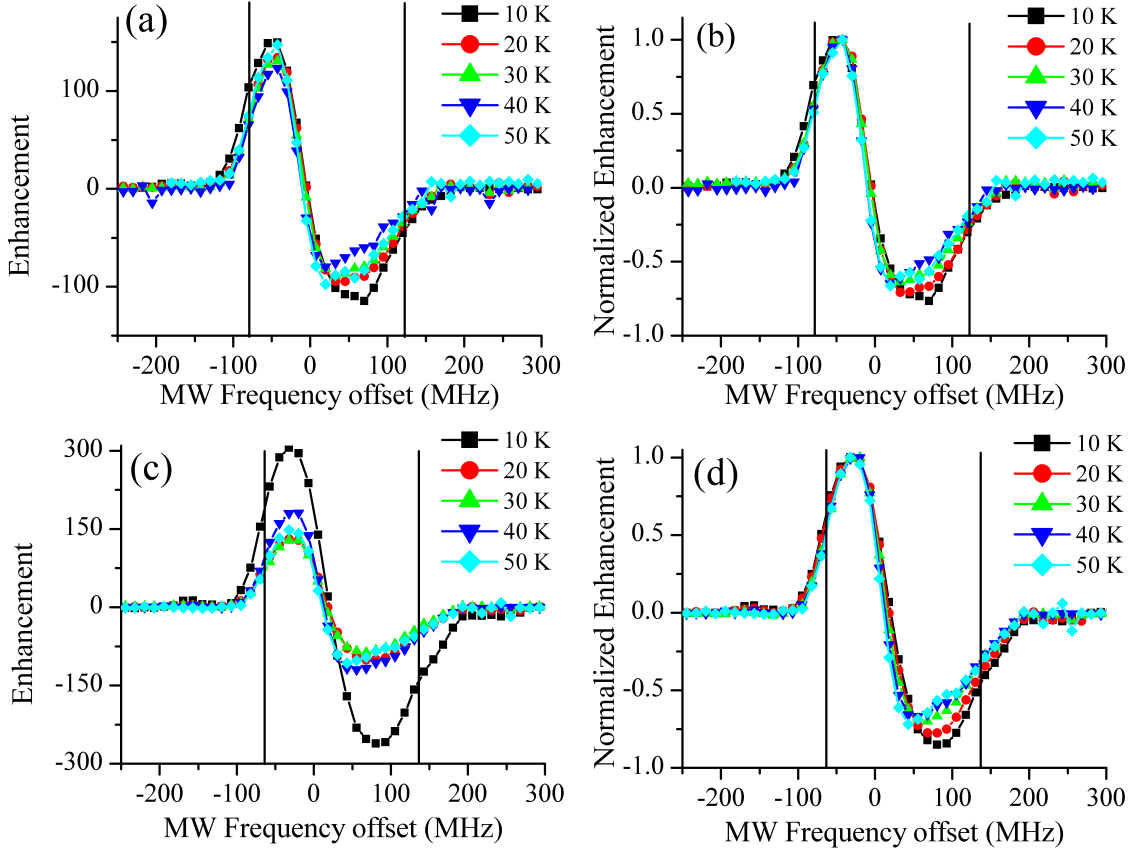
Fig. 4: DNP spectra in the range of 10-50 K of Radical 1 in ^{13}C glycerol-water (50/50), given with respect to 94.825 GHz shown in absolute enhancement (a) and normalized to ease comparison of the lineshapes (b). (c), (d) the same for Radical 2 in ^{13}C Glycerol-water (50/50) given with respect to 94.878 GHz. The vertical lines represent the edges of the EPR spectrum. The irradiation times are specified in the experimental section and in Table 1.

Typical ^{13}C DNP spectra of Radical 1 and Radical 2 recorded at various temperatures are shown in Fig. 4 (a,c). These spectra were collected after MW irradiations times shorter than necessary for reaching steady state enhancements (see experimental section and Table 1). A few measurements carried out under steady state conditions showed that these lineshapes did not deviate from the steady state lineshapes. Maximum steady state enhancements of about 250 ± 20 were observed at 20 K with an irradiation time of $T_{DNP} \approx 2800$ s, which is significantly longer than the buildup time constant $T_{bu} \approx T_{1n} \approx 500$s for both Radical 1 and Radical 2.

In the present work we are mostly interested in variations in the DNP lineshapes. Accordingly, to ease the comparison of the DNP lineshapes we present normalized spectra of Radical 1 and 2 in Figs. 4 (b and d, respectively). For both radicals we observe a change in the DNP spectra, both in the total width and lineshape, with temperature. As the temperature is lowered the DNP spectra broaden and their minima and maxima shift to higher and lower

11

MW frequencies, respectively. This is particularly visible for the minima of the DNP spectra that shift from 10 MHz at 50 K to 70 MHz at 10 K for Radical 1 and from 45 MHz to 90 MHz for Radical 2. Similarly, the DNP maxima shift with temperature toward lower frequencies, though to a lesser extent.

Table 1: Maximum Enhancement Data of Radical 1 and 2.

Temperature (K)	10	20	30	40	50
Enhancement (irradiation time) Radical 1	149 ± 12 (600 s)	133 ± 11 (600 s) 250 ± 20 (steady state)	130 ± 10 (600 s)	123 ± 10 (800 s)	147 ± 12 (1200 s)
Enhancement (irradiation time) Radical 2	297 ± 24[a] (800 s)	131 ± 11 (600 s) 250± 20 (steady state)	128 ± 11 (600 s)	181 ± 16 (800 s)	148 ± 12 (800 s)

[a] The significantly higher enhancement as compared to Radical 1 at 10K is attributed to the longer MW irradiation time.

DNP lineshape microwave power dependence

We have also investigated the dependence of the DNP lineshape on the MW power, as shown in Fig. 5. By lowering the microwave irradiation amplitude from 0.6 MHz to 0.06 MHz, while keeping the irradiation time constant, we observed an expected reduction of the enhancement. However, together with this reduction a significant narrowing of the spectra is clearly detected. Both the temperature and power dependent DNP lineshapes suggest that there is a change in the relative contribution of the SE- and CE-DNP mechanisms. In the next section we present simulations of SE - and CE - DNP spectra that reproduce the main features of the DNP spectra, substantiating this observation.
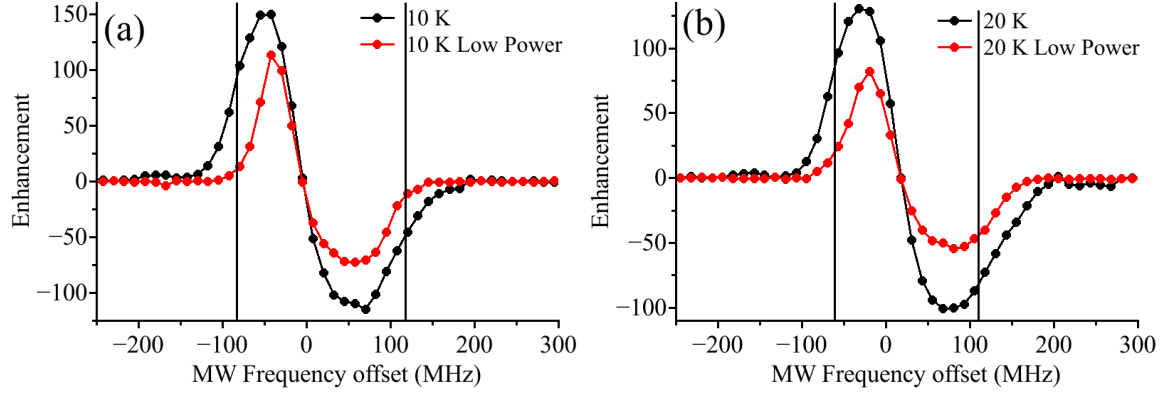
Fig. 5: DNP spectra of (a) Radical 1 at 10 K, high MW power (black, $\omega_1/2\pi \approx 0.6$ MHz) and low MW power (red, $\omega_1/2\pi \approx 0.06$ MHz); (b) Radical 2 at 20 K high MW power (black) and low MW power (red). The power is the same as in (a).

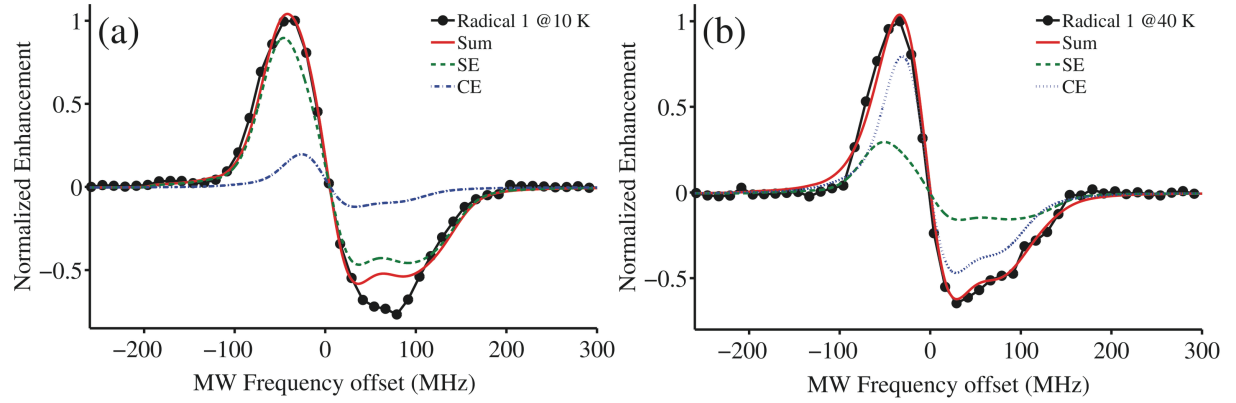## DNP spectral analysis

Temperature dependence

Fig. 6: DNP spectra of Radical 1 at 10 K (a) and at 40 K (b) with high MW power (black) compared with simulations using model I: SE in green, CE in blue, and sum in red.

Initially we simulated the spectra using model I. After creating the basic SE and CE spectra, the DNP spectrum at each temperature was fit by a superposition of these SE and CE spectra with different relative amplitudes. Fig. 6 presents the simulations of the high microwave power DNP spectra of Radical 1 at 10 K (Fig. 6a) and 40 K (Fig. 6b)). The parameters used in the simulations are given in the experimental section. These simulations show that at 40 K the CE dominates and the agreement between the experimental and calculated spectra is very good. Analysis of the 10 K spectrum shows that the SE-DNP lineshape dominates, but the fit is not as good as for the 40 K spectrum. While the total linewidth and most of the features are reproduced, we do observe a discrepancy in the negative part of the DNP spectrum. This

discrepancy is observed in all spectra where there is a significant contribution of the SE-DNP lineshape, as shown in the supplementary information, Fig. S2. These simulations show that the CE dominates the spectra in the high temperature range and the SE at the low temperature range. Based on these fits, Fig. 7 depicts the evolution of the relative contribution of the CE-DNP and SE-DNP spectra to the experimental DNP spectra as a function of temperature. For Radical 1 the CE portion drastically increases in the range from 20 to 40 K, while the SE contribution goes down.
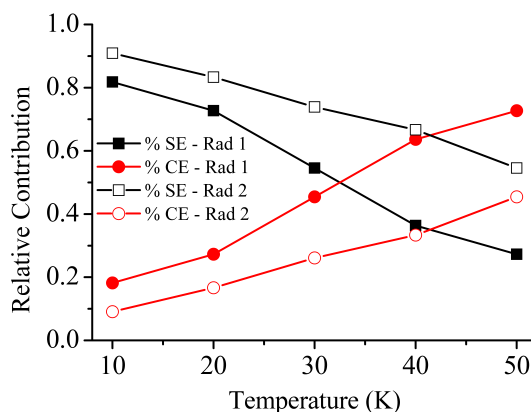

Fig. 7: The temperature evolution of the contribution of SE (black) and CE (red) to the DNP spectra. Full symbols correspond to Radical 1, open symbols for Radical 2.

The DNP spectra of Radical 2 were analyzed in a similar way and Fig. 8 presents the fits obtained for the DNP spectra at 20 and 40 K. Again, the fit of the 40 K spectrum is better than that of the 20 K spectrum. As for Radical 1, the main discrepancy is again in the negative part of the DNP spectrum. Simulations of all other DNP spectra are presented in Fig. S3 in the SI. Similar to Radical 1, and again ignoring the small deviations around 70 MHz, we observe a gradual change in the proportion of SE and CE contributions, as shown in Fig. 7. The SE contribution decreases continuously while CE increases as the temperature is increased. Interestingly, Radical 2 has a larger SE contribution throughout the temperature range measured.
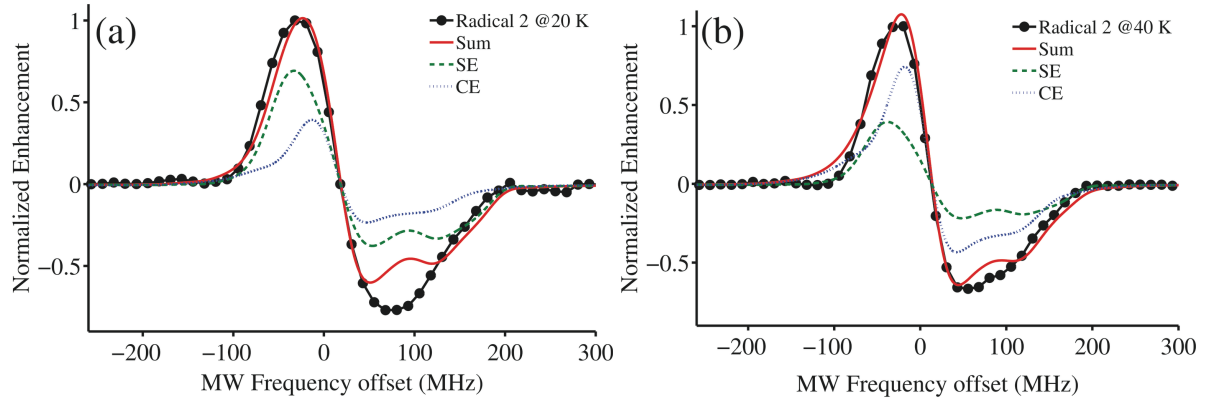
14

Fig. 8: DNP spectra of Radical 2 at 20 K (a) and at 40 K (b) with the maximum MW power (black line, $\omega_1/2\pi \approx 0.6$ MHz), and comparison with the corresponding simulations with method I: SE in green, CE in blue, and sum in red.

MW power dependence

We carried out the same analysis on the low power DNP spectra. These spectra have a narrower width and a different lineshape than the high power spectra. The simulations, taking into account a lower microwave power, are presented in Fig. 9a for Radical 1 at 10 K. The total linewidth is well reproduced at the low microwave frequency domain, but again, the negative DNP part is only partially reproduced. Nonetheless, these fits indicate a suppression of the SE-DNP and an increase of the CE-DNP effect when compared to the high power spectra. The results on Radical 2, shown in Fig. 9b, are similar to those of Radical 1. The 20 K low power DNP spectrum could also be fitted by a combination of SE and CE lineshapes and again the CE is higher when low power is used as compared to the high power case.
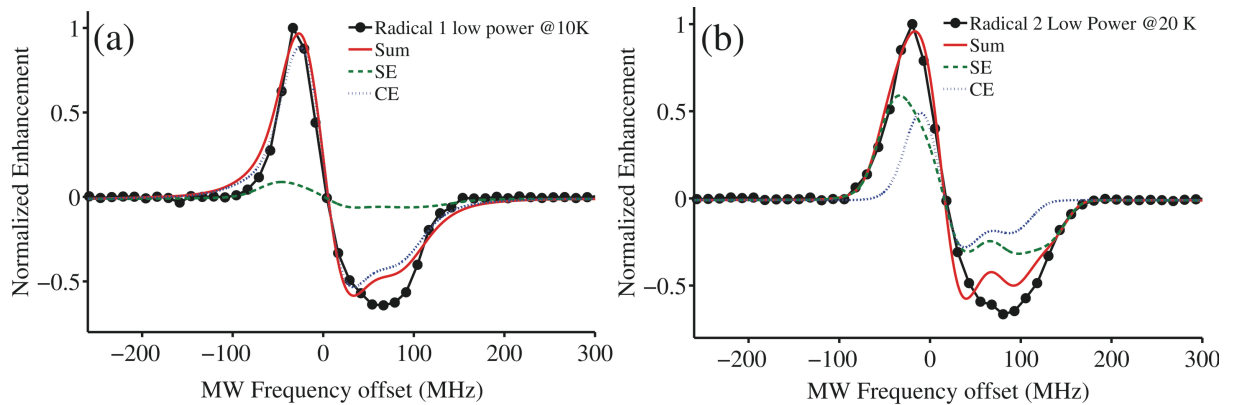

Fig. 9: DNP spectra with low MW power (black line, $\omega_1/2\pi \approx 0.06$ MHz), and simulations with method I: SE in green, CE in blue, and sum in red, (a) for Radical 1 at 10 K and (b) for Radical 2 at 20 K.

The power dependent measurements show that lowering the MW amplitude results in an overall reduction of the enhancements. The SE – CE deconvolution however reveals that while the SE contribution weakens significantly the CE contribution increase. This demonstrates the possibility of controlling the relative contributions of the two mechanisms by changing the microwave power. The absolute enhancement of the CE for Radical 1 went up from 27 to 97 by reducing the power. For Radical 2, the change is from 38 to 46. This shows that the suppression of SE leads to an increase in CE.

The simulations performed with model I provided a general description of the DNP processes that underlie the DNP enhancement with the perchlorinated trityl derivatives. The DNP lineshape analysis seems to be appropriate at the high temperature range, but as the temperature decreases an increasing discrepancy between the experimental and the calculated spectra is obtained at the negative part of the DNP profile. This presumably is a result of the fact that the basic SE spectrum, dominating the DNP processes at low temperatures, does not exhibit the appropriate lineshape. Despite many attempts to fit the data by changing simulation parameters, such as relaxation times and magnetic interaction parameters, this model always failed in generating an SE spectrum that when added to the CE spectrum could reproduce the low temperature lineshapes. This suggests the presence of an additional mechanism that contributes to the ^{13}C enhancement via the SE, which is discussed next.

SE-DNP simulations in the presence of ^{35,37}Cl

In our previous publication [24] we suggested that the ^{35,37}Cl nuclei of the radicals play a role in the DNP process by transmitting their hyperpolarization to the surrounding ^{13}C nuclei via ^{35,37}Cl-^{13}C dipolar couplings. The latter process is facilitated by frequency matching between some of the ^{35,37}Cl nuclear transitions and the ^{13}C transitions, which are at the ^{13}C Larmor frequency. In order to investigate this two-step polarization mechanism we simulated ^{13}C SE-DNP spectra by applying the theoretical approach presented in [4] on a three-spin system {e$^-$-^{35,37}Cl-^{13}C}. As mentioned earlier, ^{13}C DNP spectra for different orientations of the three-spin system in the external magnetic field were calculated, considering their full Hamiltonian and relaxation parameters, and added to produce a powder DNP spectrum. In these (model II) calculations the EPR lineshape is intrinsically included in the powder simulations as opposed to its convolution with calculated 2D enhancement maps in model I. The DNP enhancement calculations with model II are more rigorous quantum mechanically than those performed in [24] as they takes into account relaxation and actual dipolar interaction between ^{35,37}Cl and ^{13}C nuclei.

The computational details of the model and the values of the spin parameters were already discussed in the Experimental section. In Fig. 10 we plot two simulated 10 K SE-DNP powder spectra for (e-^{35}Cl-^{13}C) in (a) and (e-^{37}Cl-^{13}C) in (b) for the spin Hamiltonian parameters of Radical 1. These spectra are the sum (1:1) of the individual powder spectra obtained by considering the published quadrupole tensor parameters of the *ortho* and *meta* chlorine nuclei[33]. These two new theoretical lineshapes exhibit features that clearly differ from the shape obtained from model I. The ^{35}Cl lineshape resembles the experimental DNP lineshape whereas the ^{37}C lineshape deviates significantly. The differences between the results of the ^{35}Cl and ^{37}Cl calculations are attributed to the differences in their spin Hamiltonian parameters and in particular the nuclear quadrupole parameters leading to different orientation dependences of the ^{35,37}Cl transitions and their matching to the ^{13}C transitions.

To explore the effect of the strength of the quadrupolar interaction, we modified slightly the DFT predicted principal values by increasing and decreasing them by constant factors varying between 0.9 to 1.2. The resulting DNP spectra presented in Fig. 10c are a superposition of computed DNP powder spectra for each site (*ortho* and *meta*, the detailed DNP spectra are presented in Figure S4), and for both isotopes, summed according to their relative abundance [^{35}C]:[^{37}Cl]=3:1. As one can see, the values of the quadrupolar parameters have a significant effect on the shape of the calculated spectrum.
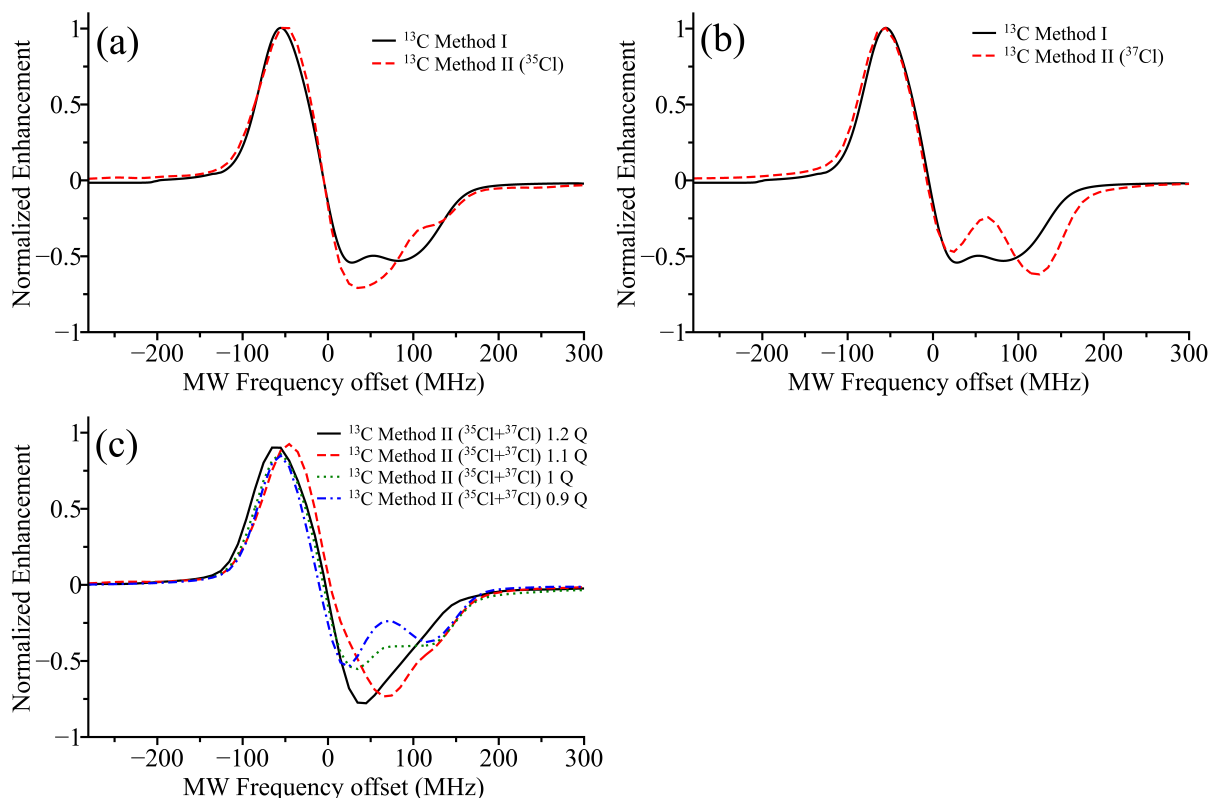
Fig. 10: DNP spectra simulated by method I and II for Radical 1 (a) SE-DNP spectrum obtained by method I (black), and the SE-DNP spectrum with method II after summing the contributions of the ortho and meta ^{35}Cl isotope (red). In (b) same as (a) with the ^{37}Cl isotope. In (c) the SE-DNP spectrum obtained after scaling the nuclear quadrupole principal values as noted on the figure; each spectrum represents the sum of the *ortho* and *meta* contributions of both isotopes.

In Fig. 11 we plot the experimental curve at 10 K, the fit obtained by method I and with method II with the quadrupole interaction scaled by 1.1, and by their combined contribution to the SE with a 1:1 relative contribution.
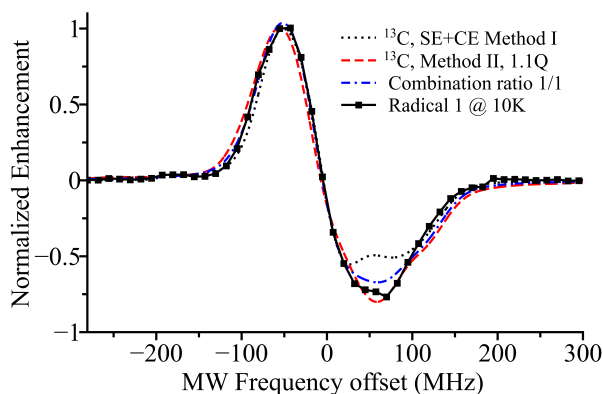

Fig. 11: Experimental DNP spectrum for Radical 1 at 10 K (line + scatter) and DNP spectra simulated by method I (23% CE + 77% SE) (black line), by method II (red), which is the sum of all chlorine contribution (*ortho, meta*, ^{35}Cl and ^{37}Cl) and scaling of the quadrupole interaction by a factor of 1.1. The sum (1:1) of both mechanisms contribution to SE (77%) is represented by the blue line.

18

It can be seen that a slight increase in the quadrupolar principal values (+10 %) predicted by DFT [24] causes narrowing and an intensity increase of the negative region of the DNP spectra, resembling more the experimental spectra.

In an effort to show a possible influence of the ^{35,37}Cl-^{13}C indirect hyperpolarization process on the actual ^{13}C-DNP spectra we concentrated on the experimental DNP spectra of Radical 1 at 10 K. This spectrum was analyzed e as composed of ~77% SE-DNP and ~23% CE-DNP contributions. A possible scenario for improving the analysis is to add a contribution to the spectrum from the indirect process. For simplicity we modified the basic SE-spectrum by combining model I and model II in a 1:1 ratio, and kept the SE- and CE-ratios as above. The result of this addition is shown in Fig. 11, demonstrating indeed a better agreement with the experiment. This supports the possibility that the ^{35,37}Cl nuclei play a role in the DNP mechanisms of the chlorinated radicals.

Discussion

In this study we focused on the characteristics of the DNP spectra and the mechanisms that contribute to the enhancement of ^{13}C by varying two parameters: the temperature and the MW power. We begin by assuming that the major contribution of the DNP enhancement comes from SE and CE polarization transfer processes from the electron spins to the local ^{13}C nuclei, followed by homonuclear spin diffusion transferring the local polarizations to the bulk nuclei[16]. Using previously developed methods, we analyzed the temperature and power dependence of the DNP spectra for both radicals. We decompose the DNP spectra into SE- and CE-DNP contributions, and overall we observed a decrease of the SE contribution as the temperature was raised. This is in good agreement with the previously published results from samples with TEMPOL, TOTAPOL and OX63[14–16]. Some of the parameters that determine the DNP efficiency are ω_1, T_{1e}, T_{2e}, T_{1n}, the radical concentration and the EPR lineshape. According to the theoretical work of Hovav et al, the SE and CE mechanisms have a somewhat different dependence on these parameters[32,33]. For best CE efficiency one needs $\frac{\omega_{1eff}^2 T_{2e}}{1+(T_{2e}\Delta\omega)^2} > \frac{1}{T_{1e}}$, where $\Delta\omega$ is the off resonance with respect to the allowed single quantum transition and T_{2e} is the radicals spin-spin relaxation. $\omega_{1eff} \approx \omega_1$ because of the CE-mixing.[32] In contrast the SE efficiency requires $\frac{\omega_{1eff}^2 T_{2e}}{1+(T_{2e}\Delta\omega)^2} > \frac{1}{T_{1n}}$, where $\Delta\omega$ is the off resonance with respect to the forbidden double (DQ) and zero quantum (ZQ) transitions and

the MW irradiation does not excite the single quantum allowed transition. $\omega_{1eff} < \omega_1$ as it includes the transition probability of the forbidden ZQ and DQ transition [32,33]. This shows that the CE and SE have different dependencies on MW power and T_{1e} and T_{1n}. As T_{1n} gets longer, the SE becomes more efficient, whereas for CE this depends on T_{1e}. However, as the detailed dependence is not known, and factors such as spectral diffusion, in particularly in the CE case, are not taken into account, it is not obvious why the CE contribution is reduced with temperature. We also noticed that in general the SE contribution is higher for Radical 2 as compared to Radical 1. Currently we cannot attribute it to a particular parameter, they differ slightly in their T_M and T_{1e} values but could also differ in their ω_{1eff}^2 values because of the different number of Cl that can affect the effective approach distance of the ^{13}C nuclei in the glycerol.

We also observed that by reducing the MW power it is possible to reduce the dominant SE contribution at low temperatures and increase the CE contribution. This finding suggests the existence of a competition between the two mechanisms, where at high power (and low temperatures) the SE takes over and suppresses the CE. This opens the possibility to enhance one mechanism at the expense of the other. This is consistent with the involvement of forbidden EPR transitions in the SE, which require high power to be efficient, while the CE needs lower power as it is driven by allowed EPR transitions. When the SE is suppressed the spin diffusion originating from CE active electrons has a better chance to spread the polarization through sample with less competition from the SE – active electrons[16]. Interestingly, a recent DNP study at 197 GHz using OX63 as a polarizer for ^{13}C pyruvate below 35 K, showed that the dominating mechanism is the CE[21]. This is consistent with our observation, especially considering the low power used in the study and that the transition probabilities of forbidden transitions (ZQ and DQ in the DNP nomenclature) at higher fields are lower, hence the SE-DNP is expected to be inefficient.

The analysis we just described is based on a model (model I) that involves only e – ^{13}C transfer. At low temperatures the simulation of the SE-DNP could not reproduce well enough the lineshape at the high frequency part of the DNP spectrum. To improve the fit we developed an additional model (model II) that takes into account the presence of ^{35,37}Cl nuclei as participants in the DNP process as proposed earlier[22–24] and termed "hetero-nuclear assisted DNP". In this mechanism the polarization transfer is calculated in a small spin system including a hyperfine-coupled ^{35,37}Cl nucleus, which is dipolar coupled to a ^{13}C nucleus. The

simulations show a buildup of polarization on the ^{13}C nucleus which can then be transferred to the surrounding ^{13}C bulk nuclei through homonuclear spin diffusion. This model seems to reproduce more accurately the DNP lineshape, in particular the higher symmetry between the positive and negative part of the DNP spectrum. In a real sample, we think that this modified mechanism can be present, in particular at low temperatures where the nuclear T_{1n} are longer although the direct electron spin to ^{13}C polarization process should be, at least theoretically, more efficient. It is reasonable to assume that a similar pathway of polarization transfer from the $^{35/37}$Cl to the ^{13}C may exist also for the CE mechanism. This could have been investigated by calculating the polarization pathway in a system like {e - e – ^{35,37}Cl - ^{13}C}; however, it was not done because of the complexity of the system. Additionally, as the basic CE-DNP lineshape fitted reasonably well the experimental lineshape acquired at the high temperature range we believe that it is less crucial.

The question that arises next is whether such a hetero-nuclear assisted DNP mechanism can contribute to ^{13}C polarization with TEMPOL or TOTAPOL via the ^{14}N nuclei. The ELDOR detected NMR spectrum of nitroxides, that maps the ^{14}N nuclear frequencies, shows at 95 GHz some weak overlap with the ^{13}C Larmor frequency at the spectral region of g_y spanning 12 mT (~360 MHz) so in principle there may be some contributions. This would have to be checked by measuring and analyzing the ^{13}C DNP spectra of TEMPOL. However, because the spectral width of the nitroxide spectrum allows efficient polarization of the ^{1}H nuclei, high ^{13}C polarization can achieved via cross-polarization[13,34,35] also in static solid DNP, therefore the direct ^{13}C polarization may be less relevant.

Finally it is interesting to compare the DNP performance of the chlorinated trityls with that of OX63 under the same conditions. Our earlier study[15] gave a maximum enhancement of 380 at 20 K for 15 mM OX63 and 6 M ^{13}C urea in DMSO/H$_2$O (50% v/v), achieved after a 1800 sec irradiation[15]. For Radical 1 in 10 mM in glycerol-1,3-^{13}C/H$_2$O (50/50 % in volume) we obtained at 20 K a maximum enhancement of 250, achieved after 2000 s irradiation time. Considering the broader EPR spectrum (factor of ~3.5) and the lower concentration, these radicals seem to be quite efficient polarizers in the solid state. Their lower stability due to light sensitivity, which requires careful storage conditions, is however a significant drawback.

Conclusions

The ^{13}C-glycerol DNP spectra of two chlorinated Trityl radicals were found to be both temperature and power dependent. Analysis of the DNP lineshape, in terms of a superposition of basic SE- and CE- DNP lineshapes, which takes into account electron and nuclear spin relaxation times, but neglects electron spin spectral diffusion and nuclear spin diffusion, reproduced sufficiently well the spectra of the high temperature range (40 - 50 K), but less so the spectra of the low temperature end (10 - 20 K). The CE mechanism prevailed under conditions of low power and high temperature, while the SE dominated at low temperatures and high power. This seems to be a rather general behavior as it has been observed earlier for ^{13}C DNP with OX63 and ^{1}H DNP with TEMPOL and TOTAPOL. The agreement between the calculated spectra and the experimental spectra in the low temperature end was significantly improved by taking into account explicitly the presence of ^{35,37}Cl nuclei as participants in the SE-DNP process thus further supporting the existence of "hetero-nuclear assisted DNP".

Supporting information available

Simulations of the EDEPR, description of spin counting experiments, temperature dependent DNP spectra and their simulations using method I, calculated DNP spectra obtained with method II for the individual types of ^{35,37}Cl.

References

1. A. Overhauser, *Phys. Rev.*, 1953, **92**, 411–415.

2. A. Abragam, *Phys. Rev.*, 1955, **98**, 1729–1735.

3. C. D. Jeffries, *Phys. Rev.*, 1957, **106**, 164–165.

4. Y. Hovav, A. Feintuch, and S. Vega, *J. Magn. Reson.*, 2010, **207**, 176–189.

5. K.-N. Hu, G. T. Debelouchina, A. A. Smith, and R. G. Griffin, *J. Chem. Phys.*, 2011, **134**, 125105.

6. A. Karabanov, A. van der Drift, L. J. Edwards, I. Kuprov, and W. Kockenberger, *Phys. chem. chem. phys.*, 2012, **14**, 2658–68.

7. C. Hwang and D. Hill, *Phys. Rev. Lett.*, 1967, **19**, 1011–1014.

8. C. Hwang and D. Hill, *Phys. Rev. Lett.*, 1967, **18**, 110–112.

9. Y. Hovav, O. Levinkron, A. Feintuch, and S. Vega, *Appl. Magn. Reson.*, 2012, **43**, 21–41.

10. A. Karabanov, G. Kwiatkowski, and W. Kockenberger, *Appl. Magn. Reson.*, 2012, **43**, 43–58.

11. A. Abragam and M. Borghini, in *Progress in Low Temperature Physics*, 1964, pp. 384–449.

12. A. Abragam and M. Goldman, *Reports Prog. Phys.*, 1978, **41**, 395–467.

13. S. Jannin, A. Bornet, S. Colombo, and G. Bodenhausen, *Chem. Phys. Lett.*, 2011, **517**, 234–236.

14. D. Shimon, Y. Hovav, A. Feintuch, D. Goldfarb, and S. Vega, *Phys. Chem. Chem. Phys.*, 2012, **14**, 5729–43.

15. D. Banerjee, D. Shimon, A. Feintuch, S. Vega, and D. Goldfarb, *J. Magn. Reson.*, 2013, **230**, 212–9.

16. D. Shimon, A. Feintuch, D. Goldfarb, and S. Vega, *Phys. Chem. Chem. Phys.*, 2014, **16**, 6687–99.

17. J. H. Ardenkjaer-Larsen, S. Macholl, and H. Johannesson, *Appl. Magn. Reson.*, 2008, **34**, 509–522.

18. J. H. Ardenkjaer-Larsen, B. Fridlund, A. Gram, G. Hansson, L. Hansson, M. H. Lerche, R. Servin, M. Thaning, and K. Golman, *Proc. Natl. Acad. Sci. U. S. A.*, 2003, **100**, 10158–63.

19.   J. Wolber, F. Ellner, B. Fridlund, A. Gram, H. Johannesson, G. Hansson, L. H. Hansson, M. H. Lerche, S. Mansson, R. Servin, M. Thaning, K. Golman, and J. H. Ardenkjaer-Larsen, *Nucl. Instrum. Meth. A*, 2004, **526**, 173–181.

20.   A. A. Smith, B. Corzilius, J. A. Bryant, R. Derocher, P. P. Woskov, R. J. Temkin, and R. G. Griffin, *J. Magn. Reson.*, 2012, **223**, 170–9.

21.   S. a Walker, D. T. Edwards, T. A. Siaw, B. D. Armstrong, and S. Han, *Phys. chem. chem. phys.*, 2013, **15**, 15106–20.

22.   C. Gabellieri, V. Mugnaini, J. C. Paniagua, N. Roques, M. Oliveros, M. Feliz, J. Veciana, and M. Pons, *Angew. Chem. Int. Ed. Engl.*, 2010, **49**, 3360–2.

23.   J. C. Paniagua, V. Mugnaini, C. Gabellieri, M. Feliz, N. Roques, J. Veciana, and M. Pons, *Phys. chem. chem. phys.*, 2010, **12**, 5824–9.

24.   D. Banerjee, J. C. Paniagua, V. Mugnaini, J. Veciana, A. Feintuch, M. Pons, and D. Goldfarb, *Phys. Chem. Chem. Phys.*, 2011, **13**, 18626–37.

25.   N. Roques, D. Maspoch, K. Wurst, D. Ruiz-Molina, C. Rovira, and J. Veciana, *Chemistry*, 2006, **12**, 9238–53.

26.   D. Maspoch, N. Domingo, D. Ruiz-Molina, K. Wurst, G. Vaughan, J. Tejada, C. Rovira, and J. Veciana, *Angew. Chem. Int. Ed. Engl.*, 2004, **43**, 1828–32.

27.   A. Feintuch, D. Shimon, Y. Hovav, D. Banerjee, I. Kaminker, Y. Lipkin, K. Zibzener, B. Epel, S. Vega, and D. Goldfarb, *J. Magn. Reson.*, 2011, **209**, 136–41.

28.   D. Goldfarb, Y. Lipkin, A. Potapov, Y. Gorodetsky, B. Epel, A. M. Raitsimring, M. Radoul, and I. Kaminker, *J. Magn. Reson.*, 2008, **194**, 8–15.

29.   S. K. Zaremba, *Ann. di Mat. Pura ed Appl. Ser. 4*, 1966, **73**, 293–317.

30.   H. Conroy, *J. Chem. Phys.*, 1967, **47**, 5307–5318.

31.   V. B. Cheng, H. H. J. Suzukawa, and M. Wolfsberg, *J. Chem. Phys.*, 1973, **59**, 3992.

32.   Y. Hovav, A. Feintuch, and S. Vega, *J. Chem. Phys.*, 2011, **134**, 074509.

33.   Y. Hovav, A. Feintuch, and S. Vega, *J. Magn. Reson.*, 2012, **214**, 29–41.

34.   A. Bornet, R. Melzi, S. Jannin, and G. Bodenhausen, *Appl. Magn. Reson.*, 2012, **43**, 107–117.

35.   S. Jannin, A. Bornet, R. Melzi, and G. Bodenhausen, *Chem. Phys. Lett.*, 2012, **549**, 99–102.